# Using Optical Coherence Microscopy to Study Early Frog Development

Andrew J. Schile

April 29, 2001
Senior Thesis
Advisors: M. Williams, R. Haskell & D. Petersen

Harvey Mudd College

## Abstract

We have used the non-invasive and non-destructive imaging technique of optical coherence microscopy (OCM) to document morphological changes that occur internally within the frog *Xenopus laevis* during gastrulation, a critical event in the early embryonic development of animals. OCM generates images by using interferometry to penetrate deeply within turbid tissue to measure inherent cellular light scattering properties. We have generated two-dimensional and three-dimensional time-lapse movies that depict *in vivo* motion that is consistent with the behavior of the internal migrating mesoderm during gastrulation. This achievement is noteworthy because mesodermal migration occurs at depths prohibitive to conventional light, two-photon and confocal microscopy, and also because there are no published accounts of gastrulation within a single embryo.

Light scattering theory predicts that a light source with a longer wavelength will allow for deeper scans. To verify this, we have compared images of developing embryos acquired using Harvey Mudd College's three-dimensional OCM ($\lambda$ = 843 nm) to images acquired using a similarly designed two-dimensional microscope ($\lambda$ = 1310 nm) at the Beckman Laser Institute. We have found that the longer wavelength indeed provides an enhanced depth penetration. We have also characterized the optical scattering properties of the ectoderm and mesoderm by determining how quickly the OCM signal attenuates within each tissue layer. The signal attenuations in the ectoderm ($18.3 \pm 3.0$ mm$^{-1}$) and mesoderm ($19.2 \pm 5.0$ mm$^{-1}$) agree within uncertainties, suggesting that these tissues are optically indistinguishable, at least in terms of bulk optical properties. Moreover, the mean value for both tissues at 1310 nm is $14.0 \pm 2.0$ mm$^{-1}$ (compared to $19.0 \pm 3.0$ mm$^{-1}$ at 843 nm) leading to a 36% improvement in depth penetration at the longer wavelength.

# Introduction

Optical coherence microscopy (OCM) is a powerful new tool in biological imaging, as it is a non-invasive, non-destructive technique for rapidly generating three-dimensional images of organisms *in vivo*. The applications of a similar technology, optical coherence tomography (OCT), to animal development have been demonstrated in several instances, most notably by the *in vivo* imaging of developing neural (Boppart *et al*., 1996) and cardiovascular structures (Boppart *et al*., 1997) in larvae of the frog *Xenopus laevis,* as well as of the formation of the anterioposterior axis in zebrafish embryos (Boppart *et al*., 1996). All published work on the applications of OCT or OCM to animal development has been conducted on nearly transparent embryos (zebrafish) or larvae (*Xenopus*) (Hoeling *et al*., 2000), and there are no published OCT or OCM images of structures within the highly opaque early-stage *Xenopus* embryo. Moreover, no OCM or OCT time-lapse accounts of developmental events have been published. We present results here that show the *in vivo* resolution of the internal migration of the mesoderm during gastrulation within a single embryo.

**Gastrulation: A Crucial Morphogenetic Event in Animal Development**

Gastrulation is a complex morphogenetic process that occurs in stage 10-11 *Xenopus laevis* embryos (Fig. 1). During gastrulation cellular migrations establish three distinct tissue layers, ectoderm, mesoderm and endoderm, which later give rise to all major organ systems (Keller 1975; Keller 1976). It is important to characterize the temporal and spatial relationships between these tissues over time because neurulation and other events of later development are driven by molecular signaling between adjacent tissues (for a review, see Fraser and Harland, 2000). Much of what is known about

morphogenesis during *Xenopus* gastrulation has been learned by studying sectioned embryos and by observing the behavior of isolated tissue explants (Keller, 1975; Winklbauer and Schurfeld, 1999). By fixing and sectioning embryos at different times during gastrulation, embryologists have inferred internal events based on the extent of tissue motion between successive sections. These analyses have been useful in characterizing the morphology of embryos undergoing gastrulation, but they cannot provide a complete documentation of the spatial and temporal complexities of morphogenesis.

Prior to gastrulation, *Xenopus* has a simple animal-vegetal asymmetry (Fig. 1A). The animal hemisphere is marked by the presence of the blastocoel, a fluid-filled cavity (Fig. 1A, region labeled "BLC"). The prospective ectoderm is derived from the cells of the blastocoel roof. As gastrulation proceeds they spread to cover the entire exterior of the embryo in the process of epiboly (Keller, 1980). The vegetal hemisphere consists of dense yolk cells that constitute the future endoderm (Fig. 1, shaded yellow). The mesoderm originates from epithelial and subepithelial cells in the involuting marginal zone that is located animally to the blastopore lip (Fig. 1, light orange tissues).

Although the mesoderm is derived from cells initially on the exterior of the embryo, these cells must internalize to ensure placement of mesoderm between ectoderm and endoderm (Fig. 1C). Gastrulation initiates on the vegetal surface at the dorsal blastopore lip (Fig. 1B, E). The blastopore lip is an invagination where mesodermal IMZ cells of the prospective mesoderm turn and enter the interior of the embryo in the process of involution. The blastopore lip forms as a population of cells constrict their apices along the animal-vegetal axis, thereby drawing the neighboring IMZ inward toward the

endodermal yolk mass (Heasman 1997). Recent evidence suggests that the endoderm initiates the internalization of the mesoderm by distorting itself and expanding into the blastocoel (Winklbauer and Schurfeld, 1999).

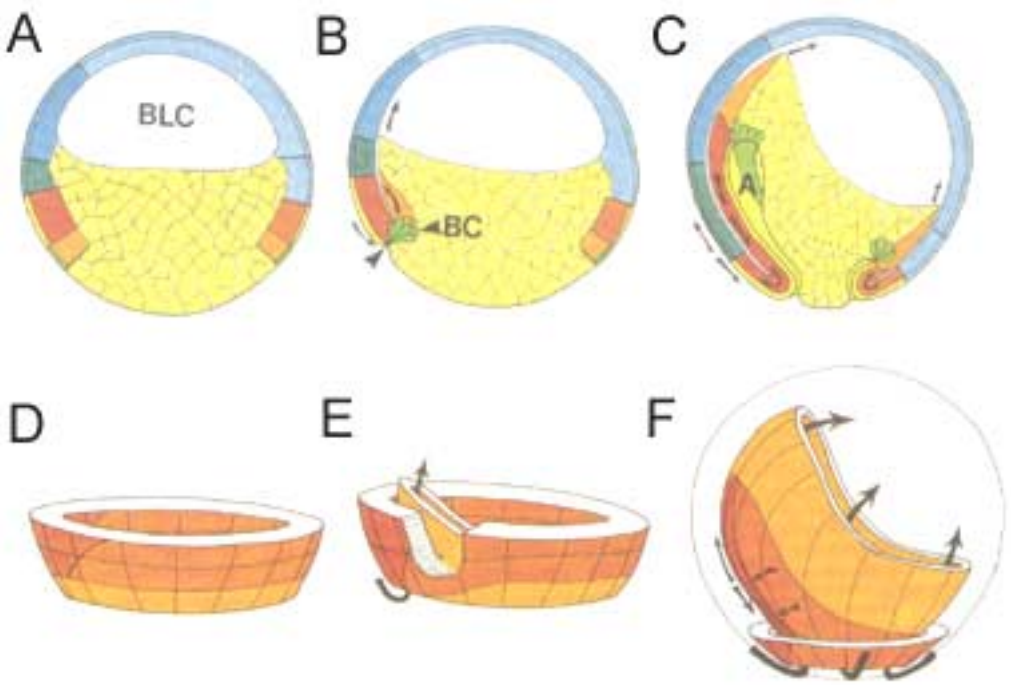


**Figure 1** Sketches illustrating internal tissue movements during gastrulation in stage 10 *Xenopus* embryos. A midsagittal view is shown chronologically in the top row (A-C) and the behavior of the mesoderm is shown in three dimensions with the same relative time scale (D-F). Dorsal is to the left and ventral is to the right. Ectoderm is shaded blue, endoderm is shaded yellow and mesoderm is shaded orange. **A**, Pregastrular embryos (stage 10) showing blastocoel (BLC), and mesoderm precursors (orange regions); **B**, Constriction of bottle cells (green, labeled BC) on the dorsal vegetal surface and involution of mesoderm; **C**, Internal migration of mesoderm occurs circumferentially around the vegetal hemisphere (stage 10.25); **D**, The mesoderm is shown prior to gastrulation. **E**, Involution and migration are most prominent from dorsal surface and it ensures placement of the mesoderm beneath the ectoderm (**F)** Adapted from Keller, 1991.

The cells that involute at the dorsal vegetal surface migrate in the dorsal-to-ventral direction along the blastocoel roof, pulling the endodermal yolk mass with it as it moves (Fig. 1C). Although mesodermal involution initiates on the dorsal side, it occurs circumferentially on the vegetal hemisphere by extending laterally and ventrally (Fig. 1 D-F). The blastopore lip ultimately forms a ring of involution that ensures the placement of mesoderm between ectoderm and endoderm (Fig. 1F). The ring of involution shrinks in size, ensuring complete internalization of endoderm as well (Fig. 1C).

**Non-Invasive Biological Imaging with Optical Coherence Microscopy**

Fixing and sectioning methods provide a workable account of gastrulation, but they require the sacrifice of many embryos as well as interpolating between fixed stages of different embryos. This is necessary because X*enopus* embryos are opaque and consequently it is not possible to readily observe internal morphologies with conventional light microscopy. Novel advances in non-invasive imaging may render these traditional methods obsolete by documenting gastrulation in real-time within a single live embryo. A non-invasive technique for studying the morphology of developing animals in real time could greatly enhance the field of descriptive embryology by providing more complete accounts of developmental events. Optical coherence microscopy (OCM), microscopic magnetic resonance imaging (μMRI), two-photon microscopy and confocal microscopy are four such imaging techniques. Although confocal, two-photon and μMRI resolve internal tissue morphologies, none is well suited to creating a real-time account of gastrulation within a single *Xenopus* embryo.

MRI microscopes are expensive and require approximately one hour to image an entire *Xenopus* embryo (C. Papan, personal communication). Since gastrulation occurs

over two to three hours, μMRI cannot follow these events in real-time. Moreover, this technique cannot readily resolve the boundaries of the blastocoel. μMRI does have advantages over optics-based microscopy because it is not limited by tissue opacity (Jacobs *et al*., 1999). Several injectible contrast agents have been developed to distinguish between tissues and to respond to gene expression (Jacobs *et al*., 1999; Louie *et al*., 2000).

Confocal microscopes are affordable and commercially available; however, depth penetration is limited to less than 100 μm within highly scattering tissue and they generally require the use of exogenous labeling agents (Herman, *et al*. 1993; Paddock, 1999). Confocal suffers from a 10-fold decrease in depth penetration as compared to OCM (Paddock, 1999). More seriously, the high intensity of the light source is quite destructive to tissue, since it generates genotoxic free radicals (Haseloff, 1999; Paddock, 1999). This limits the effectiveness of confocal microscopy in following tissues over extended periods of time *in situ*.

OCM and confocal microscopy both utilize backscattered light in reconstructing images of biological samples. The depth penetration of confocal microscopy is limited by multiple scattering, which occurs when the incident light is scattered by tissues outside of the focal plane (Fig 2A). Multiply scattered light carries no information about the tissue of interest, and this phenomenon ultimately limits the depth penetration of confocal microscopy. OCM utilizes the principles of Michelson interferometry to preferentially exclude light that has been scattered multiple times (Hoeling *et al*., 2000). This is achieved by requiring that the collected light travel a specified distance within the sample.

We use a superluminescent diode that emits low intensity (1 mW) light in the near-infrared part of the spectrum (843 nm). This light is split along one of two paths ("arms") (Fig 2B). Light in the sample arm is focused to a spot 5 μm in diameter on the tissue, and light in the reference arm is reflected by a mirror (Fig. 2B). The optical path lengths of these two arms are kept equal and an additional length is added to the reference arm to compensate for the index of refraction of the tissue being scanned. This is done to correct for any optical path length differences that are introduced as the light in the sample arm passes through the tissue (Hoeling *et al*., 2000).

The cellular components within the 5 μm spot on the tissue can scatter, absorb or transmit the incident light from the sample arm. Scattering occurs in all directions, but OCM only measures the light that is backscattered directly into the fiber optic cable of the sample arm (Fujimoto *et al*., 1998). The light scattered back by the tissue is combined at a photodetector with light from the reference arm. Constructive and destructive interference fringes appear when the mirror is oscillated over small displacements, and the root-mean-square amplitude of the fringes is proportional to the square root of the intensity of backscattered light (Hoeling *et al*., 2000). A pair of galvo-scanning mirrors moves the focused beam to measure backscattering intensities throughout the plane of focus.

Depth penetration is achieved by moving the focusing lens in the sample arm to focus the beam at a slightly greater depth within the tissue. At the same time, the reference mirror is translated away from the beamsplitter so that the equal path length position is kept coincident with the focused waist of the beam. The coincidence of the

focused waist and the equal path position ensures maximal lateral resolution throughout the imaging process. The microscope is now focused only on a single plane within the

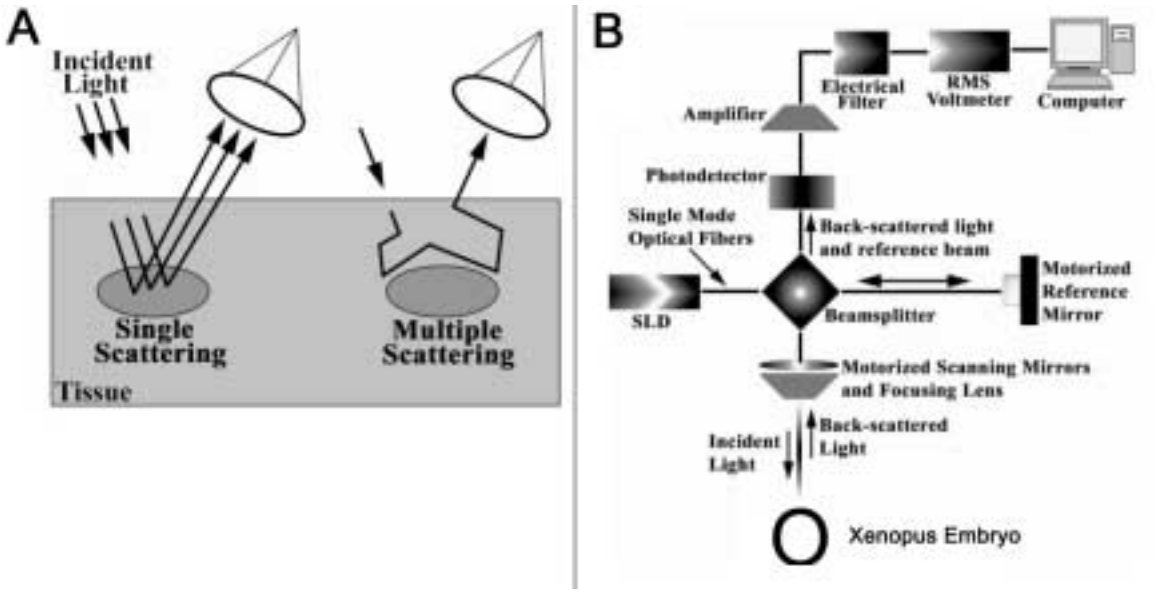


**Figure 2 A** An illustration of single versus multiple scattering. **B** A schematic of the setup of the OCM at HMC. Adapted from Hettinger, *et al*. 2000.

embryo since interferometry excludes scattering information from out-of-focus planes (Hoeling *et al*., 2000). After moving down the sample arm and incrementing the position of the mirror, the 2-D planar scan is then repeated and 3-D images are constructed by stacking together the planar scans.

The lateral resolution is given by the size of the focused beam (a spot 5 μm in diameter), and the coherence length of the light source limits depth resolution to 10 μm in tissue (Hoeling *et al*., 2000). This corresponds to a cylindrical resolution volume ("voxel") of diameter 5 μm and depth 10 μm. The spacing between sampled voxels ("step sizes") within a single planar scan and between stacked planes can be specified.

Clearer images can be obtained by specifying lateral and depth step sizes smaller than 5 μm and 10 μm, respectively, as this oversamples the tissue and thus acts to average out noise (Hettinger *et al.*, 2000; Gurses-Ozden *et al.*, 1999). Typically, lateral step sizes of 10 μm or 15 μm are used to generate large images with planar dimensions of 1 mm x 1 mm or 1.5 mm x 1.5 mm, respectively.

1.5 mm x 1.5 mm x 1.5 mm OCM images can be acquired every ten minutes and images acquired sequentially can be used to create time-lapse movies of developmental events. The acquisition time (ten minutes) is sufficiently fast to generate enough images to produce movies that approximate a real-time account of *Xenopus* gastrulation, which occurs over two to three hours at 25 C (Hausen, 1991). For example, a typical time-lapse data set that documents gastrulation (2-3 hours) will usually consist of 10-20 images taken at ten minutes intervals. Since OCM is a non-destructive imaging technique, we are able to image the same embryo throughout gastrulation with no noticeable tissue damage.

**Image Analysis and Construction of Time-Lapse OCM & OCT Movies**

Images from the OCM at Harvey Mudd are analyzed using software written for Visualization Express 5.0 (Advanced Visualization Systems, Inc., Waltham, MA). The software maps 256 colors to the scattering intensities of the voxels to generate a false-color image. The voxels that backscatter the most light are shaded red and those that scatter the least are shaded blue. Prior to opening the images in the visualization software ("AVS"), the data is histogram-stretched since the majority of voxels are of very low intensities. Stretching allows for a more dynamic range of colors in AVS. Similarly, the

two-dimensional images from the OCT at the Beckman Laser Institute are mapped either to a false-color spectrum or to a grayscale.

AVS performs "volume rendering" to visualize the 3-D OCM image on a 2-D computer screen (Hoeling *et al*., 2000). Volume rendering works by displaying each pixel on the 2-D screen as a blended sum of the intensities of voxels along a line emanating from the pixel through the 3-D image. The degree of blending (opacity) can be adjusted; for instance, a low opacity is specified if it is desirable to see the contributions from voxels far behind the outermost voxels, such as when visualizing tissue structures deep within a sample (Hoeling *et al*., 2000; Hettinger *et al*., 2000). Images can be rotated in three dimensions and also cropped along the *x*, *y*, and *z*-axes to generate optical biological sections. Time-lapse movies are created by opening images in a series of successive scans and compiling them within AVS to make Apple QuickTime or Microsoft AVI movies. These movies can be annotated using the Adobe Premiere software.

**OCM Signal Decay Within Tissue Can Be Measured By The Attenuation Coefficient**

Although the Michelson interferometer offers a ten-fold improvement in depth penetration over confocal microscopy, the general scattering and absorption of the incident light by the tissue places a limit on how deeply we may scan within a sample. The scattering and absorption properties, and consequently the signal decay, vary depending on the tissue and the wavelength of the incident light. The OCM signal falls off exponentially depending on the "attenuation coefficient", which is the sum of total scattering and absorption (Van Holde, 1971). The attenuation coefficient is a measurement of how quickly the OCM signal decays within a given tissue and it can be

determined experimentally by recording the intensities of backscattered light received from different depths within the sample.

For the light to be collected at the photodetector it must not only reach the focused plane within the sample, but it must also return without being further scattered or absorbed by intervening tissue. Since the light is traveling the same distance to the focused plane as it does in the return trip to the photodetector, the signal is therefore attenuated twice. This phenomenon may be mathematically described as:

$$Intensity \propto I_o \, e^{-2\mu \; depth} \qquad \text{Eq.1}$$

where $\mu$ is the attenuation coefficient and $I_o$ is the intensity of the incident light. However, since the OCM outputs a signal that is proportional to the square root of the intensity of backscattered light (Hoeling *et al.*, 2000), the equation reduces to:

$$OCM\ signal \propto \sqrt{Intensity} \propto \sqrt{I_o} \, e^{-\mu \; depth} \qquad \text{Eq. 2}$$

The attenuation coefficient in different tissues can be determined by fitting the OCM output signal to this decaying exponential.

**The Beckman Laser Institute's OCT: A Similar Microscope Using A Light Source With A Longer Wavelength**

The OCM at HMC is capable of resolving tissues beyond the range of depths available to confocal, two-photon, or light microscopy, since none of these imaging techniques can image beyond even the ectoderm of *Xenopus* embryos (R. Haskell and S. Potter, personal communications). Although OCM can image deeply enough to detect the blastocoel-endoderm boundary, its faint appearance suggests that it is at the limit of the range of resolvable depths at 843 nm and source power of 1 mW.

One method to improve the depth penetration of the microscope involves the use of a light source at a longer wavelength. The enhanced penetration is predicted by light scattering theory (Van Holde, 1971). In addition to absorption, one of two types of scattering, Rayleigh or Mie, can be expected when light is incident on a particle (Van de Hulst, 1981). Rayleigh scattering occurs when the size of the particle is considerably smaller than the wavelength of the incident light. This is not likely to apply in the OCM situation, however, since the predominant scatterers are likely to be nuclei and other large organelles (Mourant *et al*., 2000). Mie scattering refers to situations where the size of the scatterers is on the order of the incident light, and the amount of light that is backscattered (relative to the general forward scattering) depends on the size of the particle. The scatterers in the tissue will scatter more light at shorter wavelengths than at longer wavelengths (Van de Hulst, 1981). Since it is ultimately the general scattering and absorbance of light that attenuates the OCM signal, light at a longer wavelength should therefore attenuate the signal to a lesser degree. This should result in a smaller attenuation coefficient for the ectoderm and mesoderm when they are imaged at the longer wavelength.

One of the primary goals of this project was to investigate the appearance of images acquired using a similarly designed instrument with a light source at a longer wavelength. Such an instrument is the OCT located at the Beckman Laser Institute on the campus of UC Irvine. The OCT behaves in a similar manner to the OCM described above, but there are several principle differences between these microscopes (Izatt *et al*., 1996; Boppart *et al*., 1998). The OCT utilizes a more intense light source (~ 10 mW) at a longer wavelength (1310 nm). However, it does not maintain coincident equal path

length and focused beam positions, so to compensate partially it does not focus the incident beam to as small a focused spot. Consequently, the OCT has a worse lateral resolution (20 μm) than the OCM (5 μm).

The OCT generates two-dimensional images by first performing a depth scan, then by translating the sample arm laterally and repeating depth scans. The lateral range (~ 4 mm) allows for two embryos to be imaged side-by-side. In addition to collecting scattering information, the OCT is also configured to measure phase changes due to motion of objects parallel to the incident beam; in other words, those objects that are moving vertically in the image (Zhao *et al*., 2000). This phase shift ("Doppler shift") data is collected by repeating the same depth scan eight times and calculating the phase shifts of the scatterers throughout the sampled depth between each of the scans. The mean and variance of the phase shifts is determined at each position. The OCT outputs the phase shifts and variances in separate images.

## MATERIALS AND METHODS

### Handling of *Xenopus laevis* embryos

Albino *Xenopus laevis* embryos are acquired from a breeding colony in Dr. Scott Fraser's laboratory at Caltech. Ovulation is hormonally induced by injecting female *Xenopus* with human chorionic gonadotrophin (Wu and Gerhart, 1991). The female is gravid the following day and oocytes can be obtained by squeezing her lower abdomen. Oocytes are fertilized with sperm from testes excised from mature males (typically at 18 C). Embryos are kept in sterile rearing buffer (88.0 mM NaCl, 1.00 mM KCL, 0.41 mM $CaCl_2$, 0.33 mM $Ca(NO_3)_2$, 0.82 mM $MgSO_4$, 2.4 mM $NaHCO_3$, 10.00 mM HEPES; pH 7.4).

The fertilized oocyte is surrounded by a jelly coat in which it may freely rotate. It is therefore necessary to dissolve the coat to hold an embryo in a desired orientation for imaging. Embryos are dejellied one hour post-fertilization in a 2% cysteine hydrochloride solution (pH 8.1) (Peng 1991). The eggs are placed in the cysteine solution for 10 to 15 minutes and swirled at different intervals, rinsing periodically with rearing buffer. The loss of the jelly coat is confirmed when the eggs lie closely together, whereas eggs possessing the jelly coat are separated by the thickness of the jelly. The embryos are placed in glass screw-top vials, filled with rearing buffer and transported to HMC (for OCM imaging) or to BLI (for OCT imaging) in an insulated Styrofoam cooler. They are allowed to develop to the desired stage at the ambient lab temperature of approximately 22 º C.

**Orienting Embryonic *Xenopus* for OCM Imaging**

The embryo naturally orients itself with the animal pole facing upward because of the dense yolk in the vegetal hemisphere (Fig. 1A). A dejellied embryo may be positioned in any desired orientation by wedging it in a sample holder. The sample holder is prepared by placing a plastic mold (Fig. 3A) into molten agarose, yielding an agarose gel with wells of different widths (Fig. 3B). The embryo is held in a fixed position using the light tension provided by the walls of the well. A 5% agarose gel (GibcoBRL “Ultra Pure” agarose prepared in rearing buffer) provides sufficient force between the walls of the well to reliably hold the embryo over a long period of time. The gel is placed in a Petri dish and submerged in rearing buffer. The 1.5 mm well is generally sufficient to hold a stage 10-11 embryo in a fixed position without squeezing or distorting its spherical shape.

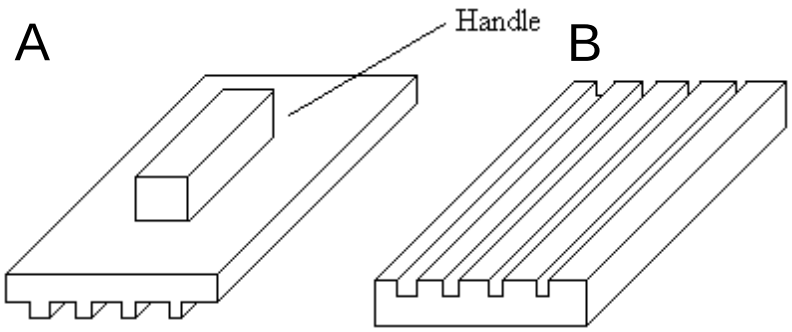


**Figure 3** Plastic mold (**A**) that is overlaid on cooling agarose to form the wells (**B**) in a sample holder for *Xenopus* embryos and larvae. Wells are 1.5, 1.4, 1.3 and 1.2 mm wide (left to right) and 2 mm deep. Drawings not to scale.

For these studies, embryos were selected for imaging if they appeared healthy and had developed appropriately, as determined by a visual inspection of cleavages. The embryos were oriented naturally with the animal pole facing upwards for imaging, and they were placed in the largest well to prevent them from drifting in the dish. The OCM introduces a compensation for the index of refraction of the frog tissue and for the rearing buffer in order to maintain a lateral resolution of 5 μm. It is necessary to maintain the air/buffer interface at a constant position since the refraction compensations are calculated from this position. Therefore, buffer was added to bring the buffer level back to the reference position approximately every fifteen minutes during the imaging session. The presence of interference fringes on an oscilloscope indicated that the buffer level was at the appropriate reference height. The embryos were imaged successively over the next several hours to capture gastrulation. At BLI OCT scanning was conducted in a similar manner, but there was no need to monitor the level of buffer in the dish since there is no correction for the index of refraction and no attempt is made to maintain a constant lateral resolution.

**Determining Attenuation Coefficients**

The attenuation coefficient is a measure of the inherent tissue scattering properties that provide the biological basis for OCM imaging. Attenuation coefficients in the ectoderm and mesoderm were determined at different points throughout gastrulation by selecting a small surface region (50 μm x 50 μm) of ectoderm that initially overlies the blastocoel, but overlies the mesoderm later in the series as the mesoderm migrates across the blastocoel roof. We have written computer programs to average the voxel intensity over the selected region for each depth in the image.

Data sets for calculating signal attenuation at various depths for the same 50 μm x 50 μm region were generated for each image in the series by outputting a spreadsheet file with scan depths in one column, average voxel intensities in the second, and the standard error of these averages in the third. We divided the data set by scan depth into ectoderm and mesoderm by assuming that the ectoderm would represent the first 140 microns of signal within the tissue. All depths beneath that were assumed to be blastocoel (prior to the migration of the mesoderm) or mesoderm thereafter. These assumptions were confirmed by visual inspection of the images. For each image in the series, the intensities throughout the top 140 microns were plotted and fitted (Eq. 2) to determine the attenuation coefficient for the ectoderm. Similarly, this value was determined in the blastocoel (early in the series) and in the mesoderm (later in the series). These values in ectoderm and mesoderm were averaged and compared to each other. To further ascertain if both ectoderm and mesoderm possess similar or the same scattering properties, an additional fit was performed in which the intensities from all depths were fitted to a single exponential.

## RESULTS

### OCM and OCT Images and Time-Lapse Movies of Gastrulation

*Xenopus* embryos were imaged throughout gastrulation using OCM at HMC on October 6/7, 2000 and February 21/22, 2001, and using OCT at BLI on February 28/March 1, 2001 (Table 1). Individual images from the February 21/22 series indicate that OCM can indeed resolve the blastocoel-yolk interface if the scans are sufficiently deep, since the blastocoel is approximately 500 μm deep at this point of development (Fig 4B). The resolution of this interface is more striking in the OCT image, presumably owing to the enhanced depth penetration of the light (Fig. 4C). Both microscopes offer a finer resolution of the ectoderm thickness than MRI microscopy can provide (S. Fraser, personal communication). However, the OCM and OCT images do not resolve fine intracellular details and the borders of the cells are not apparent. In both systems, the

**Table 1** Summary of OCM & OCT gastrulation image series

| Dates Images Were Acquired | No. of Images In The Series | Image Dimensions (mm) | Lateral step sizes (μm) | Depth step size (μm) |
|---|---|---|---|---|
| Oct 6/7, 2000 | 30 | 1 x 1 x 0.5 | 10 | 5 |
| Feb 21/22, 2001 | ~30 | 1.5 x 1.5 x 1.5 | 15 | 10 |
| Feb 28/Mar 1, 2001 | 40 | 2.56 x 4.0 [a] | 10 | 10 |

[a] Dimensions in air. The vertical dimension distorts the aspect ratio of the outputted images since there is no correction made for the index of refraction of the buffer and the embryo in the OCT images.

fluid-filled blastocoel cavity is identical in scattering intensity to the buffer in which the embryos are maintained and it does not appear to contain any prominent scatterers.

Moreover, the lower lateral resolution in the OCT images does not appear to adversely affect the image quality.

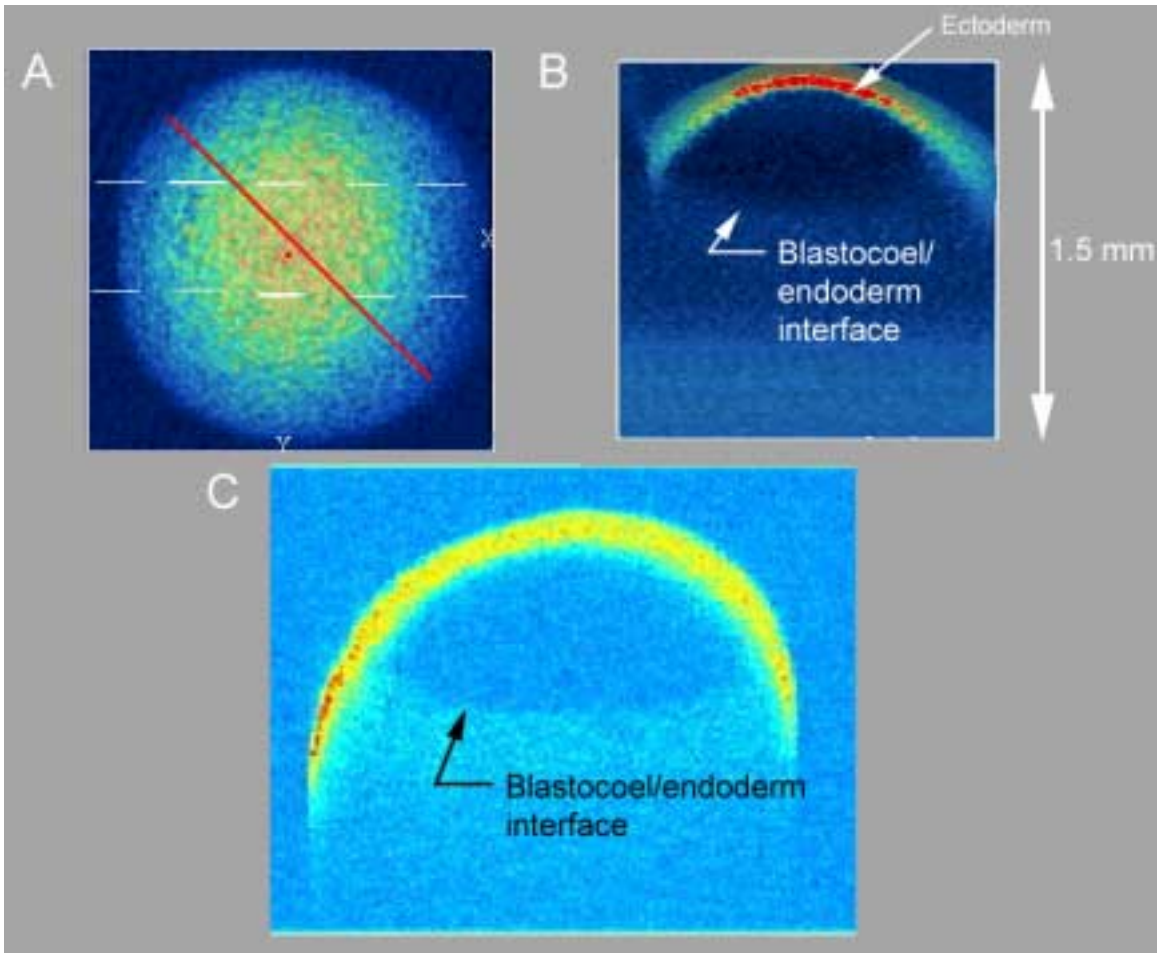


**Figure 4** Representative OCM (**A** & **B**) and OCT images (**C**) of *Xenopus* embryos at the onset of gastrulation. **A** View of the animal hemisphere of the embryo, looking down the animal-vegetal axis. The red line represents the approximate location of the dorsal midline. The white dotted lines indicate the bounds of the section shown in profile in **B**, which has a thickness of 420 μm. Gastrulation initiates on the dorsal surface, which is approximately located in the lower right portion of the image. **C** is an OCT image of a separate embryo at a comparable stage of development after scaling the image by the index of refraction (~1.4) to correct the aspect ratio. The beam is incident from the top of the image in **B** and **C.**

The image acquisition time of approximately ten minutes for 1.5 $mm^3$ scans was short enough to generate enough images to make smooth time-lapse videos that approximate a real-time account. The location of the dorsal surface was determined by inspecting the behavior of the migrating mesoderm in OCM images after the embryo was imaged (data not shown). Movies depicting the migration of the mesoderm along the blastocoel roof revealed the location of the dorsal surface (roughly in the lower right-hand corner of Fig. 4A) since migration from the dorsal portion is most prominent (Keller 1975).

The internal migration of the presumptive mesoderm is perhaps most apparent in the movie *01feb21-series-25-50-xmin45-xmax-55*. This movie was constructed by cropping each image in the series along the *y*-axis to create a 150 μm slice. This slice is not along the dorsal midline (In other words, it is not sliced like the illustrations in Fig. 1; see Fig. 4A), but the motion of the mesoderm is quite clear from this perspective. The changing appearance of the blastocoel-yolk interface can be followed for the first 60% of the movie. Initially it is quite flat, as it is attached to the migrating mesoderms, but it deforms upwards as the series progresses. Moreover, the ectoderm does not appear to thin appreciably as gastrulation progresses. The OCM movies also provide an opportunity for estimating the rate of internal migration *in vivo*. Using movies generated from the Oct 6/7 and Feb 21/22 series, we have estimated the rate of internal migration to be $3.2 \pm 0.7$ μm / min.

Analyses of these images revealed other morphologies as well. Consider, for instance, the movie *01feb21-animal48-steppingthroughy*. This movie steps through the image in thin 15 μm slices along the *y*-axis within a single image near the end of

gastrulation. One slice from the movie is duplicated here (Fig. 5A) that shows the appearance of a "pocket" within the migrating mesoderm that is devoid of scattering material. It is possible that these pockets represent a fragmenting of the blastocoel that occurs as gastrulation progresses, perhaps as the mesoderm loses contact with the ectoderm stratum in places as it migrates (S. Fraser, personal communication). These structures have also been seen in a confocal microscopy image of a fixed and optically cleared embryo (Fig. 5B) and in MRI microscopy images (C. Papan, unpublished data).

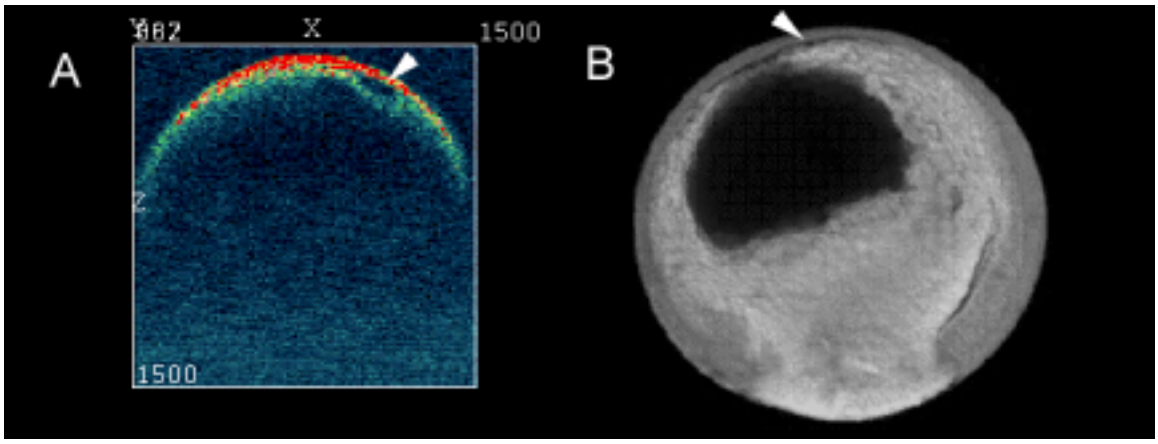


**Figure 5** Potential blastocoel fragmenting as seen in OCM and confocal microscopy images. The thinly sliced OCM image in **A** reveals the presence of blastocoel pockets (arrow) in living embryos possibly resulting from a temporary loss of adhesion between the migrating mesoderm and the ectoderm. The confocal image in **B** shows a similar structure (arrow) in a fixed embryo (Source: M. Danilchik).

These pocket structures are depicted from a different perspective in a third movie, *01feb21series-zmin14*, that was generated from the same image series. This movie was constructed by opening each image in the series, optically slicing off the top 250 μm from the animal hemisphere and looking down the animal-vegetal axis into the blastocoel (representative slices shown in Fig. 6). Initially, this perspective shows blastocoel fluid

(6A), but as gastrulation proceeds a blue crescent representing the mesoderm appears near the dorsal portion of the slice (Fig. 6B, arrow). This is consistent with the fact that mesodermal involution initiates on the dorsal surface. As gastrulation proceeds, involution proceeds ventrally as well and consequently migration occurs circumferentially around the embryo. This is indicated in the OCM image by the presence of mesoderm as a blue ring around the periphery of the slice (Fig. 6B). The blastocoel pockets are visible from this perspective as well (Fig. 6C, arrows).

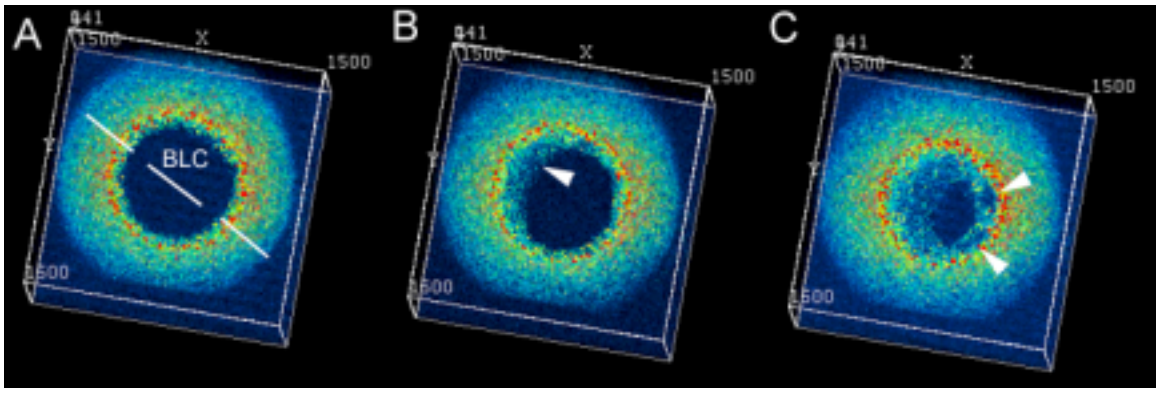


**Figure 6** Circumferential mesodermal involution about a cropped portion of the animal hemisphere. **A** Prior to gastrulation, only the blastocoel (BLC) is visible from this vantage point. **B** As gastrulation proceeds, the mesoderm is first present (arrow) along the dorsal midline (dotted line in **A**) since gastrulation initiates on the dorsal surface. **C** Late in gastrulation, mesodermal involution has occurred from both dorsal and ventral portions of the embryo, resulting in the circumferential placement of mesoderm around the slice. The arrows in **C** point to the blastocoel pockets.

The OCT movies are very informative as well. This microscope is equipped to image two embryos adjacent to one another and output three separate images that represent backscattering intensity, Doppler phase shifts of any particles moving vertically (parallel to the animal-vegetal axis) as well as the variance of the phase shifts (Fig. 7). By following the scattering images over time, it is clear that both embryos are developing

normally and undergoing gastrulation. The image on the left is oriented with the section approximately perpendicular to the dorsal-ventral axis, and the image on the right is approximately along the dorsal-ventral axis (Fig. 7A). The OCT gastrulation series clearly depicts the motion of the internal migrating mesoderm with a resolution comparable to that of the OCM images (See movies online). Additionally, the highly scattering mesoderm has shadowed the tissue beneath it (Fig. 7, arrows). The Doppler

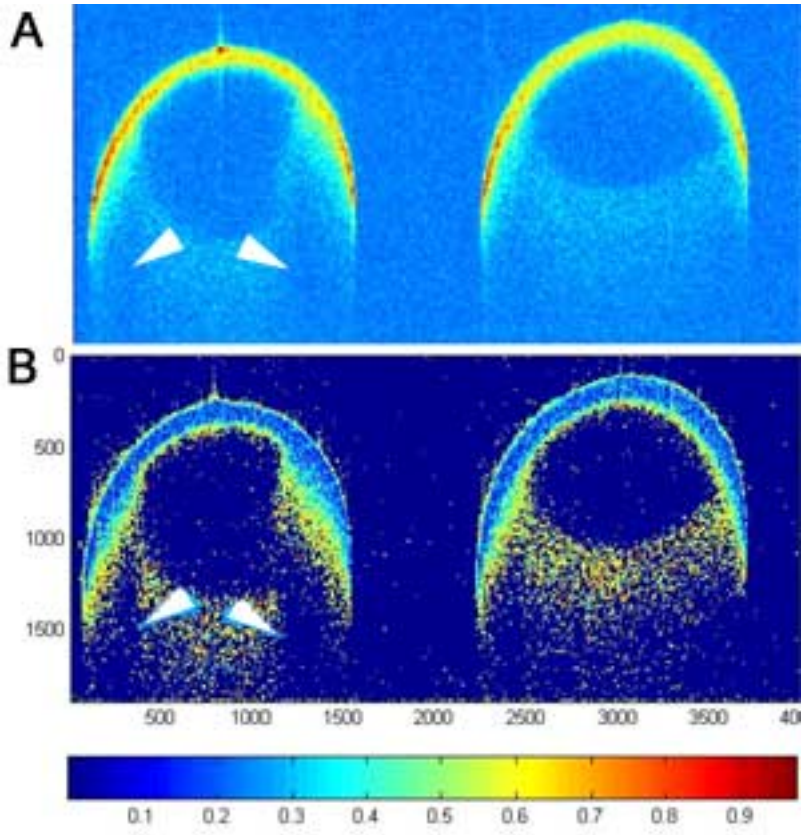


**Figure 7** Scattering intensity (**A**) and phase shift variances (**B**) can be acquired simultaneously using OCT**.** The scale bars on the image (**B**) represent microns and the scaled spectrum applies to **B** represents variance in arbitrary units. The white arrows represent shadowing owing to the mesoderm above.

phase shift images are blank (data not shown) but there is considerable Doppler phase shift variance within the endoderm, but not within the mesoderm or ectoderm, that persists throughout gastrulation (Fig. 7B). It is likely that this represents the Brownian motion of yolk platelets within the endoderm. Yolk platelets are membrane-bound vesicles comprised of phosphoproteins that constitute the energy store for the developing embryo, and their diameter (approximately one micron) is the appropriate dimension to 7be resolved by the Doppler OCT (A. Ewald & R. Haskell, personal communications).

**Similar Attenuation Coefficients In the Ectoderm and Mesoderm Suggest Similar Optical Properties During Gastrulation**

Attenuation coefficients were determined for the October 6/7 OCM series using a representative 50 μm x 50 μm x 650 μm portion (Fig. 10A) that contains ectoderm over blastocoel (Fig. 8B, left) followed by ectoderm over mesoderm once the mesoderm migrates into this field of view (Fig. 8B, right). The attenuation coefficients in the ectoderm and mesoderm were then plotted as a function of time during gastrulation (Fig. 9B). The attenuation coefficient in the ectoderm is approximately 35 $mm^{-1}$ prior to the mesoderm entering the selected region (Scan no. 20, Fig. 9B), but thereafter the coefficients in the ectoderm and mesoderm exhibit mean values of $18.3 \pm 3.0$ $mm^{-1}$ and $19.2 \pm 5.0$ $mm^{-1}$, respectively (Fig. 9B). These values agree within uncertainty, suggesting that both tissues have similar optical properties. Also, the fact that a single exponential curve fits both tissues nicely (Fig. 9A) supports this assertion.

A fit throughout the entire range of depths used (i.e., throughout the entire depth shown in Fig. 8B) yielded an attenuation coefficient of $19.0 \pm 3.0$ $mm^{-1}$ when averaged over the entire series from images 20 onward (Fig. 9B). It is not likely that the drop in

ectoderm attenuation after image 20 is owing to any physiological effect such as epiboly, which is the process in gastrulation by which the ectoderm spreads to cover the exterior

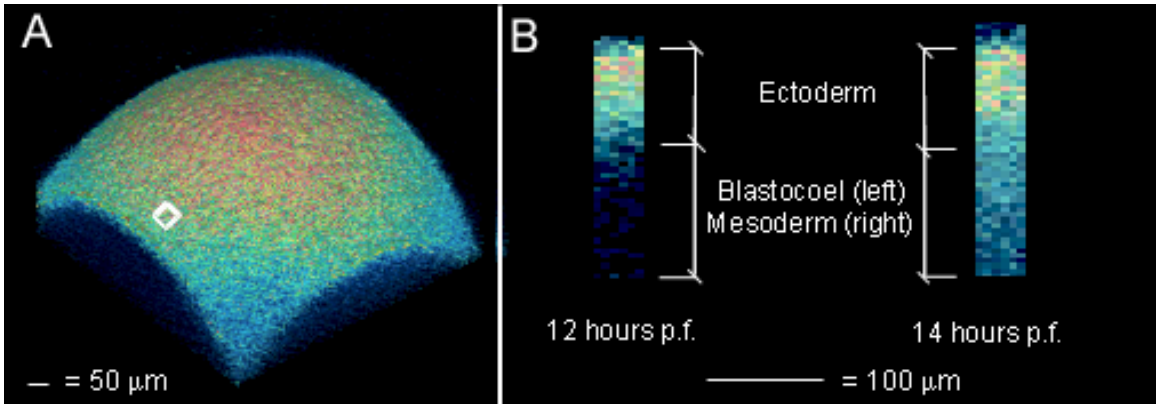


**Figure 8** Representative regions of a *Xenopus* embryo used in determining ectodermal and mesodermal attenuation coefficients during gastrulation. **A** Exterior view of the embryo showing the region depicted in cross-section in **B**. The left longitudinal section in **B** is prior to gastrulation and the same section is shown on the right two hours later, after the mesoderm has migrated beneath. Depths corresponding to the bracketed region labeled "ectoderm" were used in determining µ for the ectoderm, and depths below that were used to determine µ values for the blastocoel (12 hours post-fertilization) and mesoderm (14 hours post-fertilization).

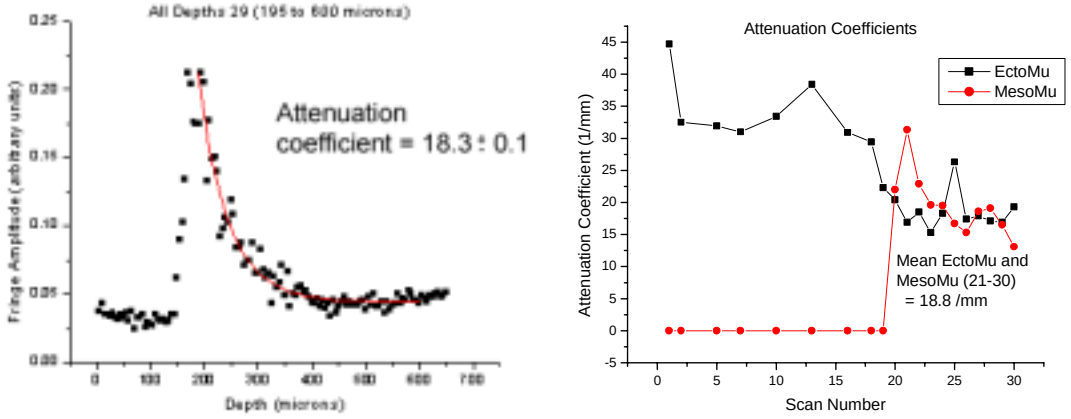


**Figure 9** Attenuation coefficients in the ectoderm, blastocoel and mesoderm throughout the October 6/7 gastrulation series. **A** Representative fit (scan 29) showing that a single exponential nicely fits both ectoderm and mesoderm. **B** Attenuation coefficients as a function of time (scans taken ten minutes apart). The boxes represent attenuation coefficients in the ectoderm and the circles represent attenuation in deeper tissues: blastocoel before scan 20 and ectoderm thereafter.

of the embryo. Rather, it is likely that our assumption that the ectoderm was 140 μm thick was an overestimate of the actual thickness. Therefore, the sharper drop off in signal intensity in the first twenty scans, and hence the higher average attenuation coefficient, could be owing to the fact that we were including blastocoel contents in the deeper portions of the ectoderm fit. The images depicted above (Figs. 4, 6 and 7) suggest that there are no prominent scatterers in the blastocoel, thus explaining the high falloff in signal in going from ectoderm to blastocoel. A lack of scatterers in the blastocoel gave very little backscattered light from the images deeper than 140 um, and the attenuation coefficients were assumed to be zero (Fig. 9B). The orientation of the embryo throughout this series did not offer a good view of the yolk cells. Consequently, an attenuation coefficient for the endoderm could not be determined from this series.

Attenuation coefficients were also calculated from 1310 nm OCT images acquired on December 20, 2000. Although these images were not acquired as part of a gastrulation series, they do indeed capture the mesoderm undergoing internal migration (Fig. 10, compare to Fig. 4 and 7). Attenuation coefficients were determined from different regions of the embryo (Fig. 10; Table 2). The average value for the attenuation coefficient at 1310 nm ($14.0 \pm 2.0$ $mm^{-1}$) suggests that the light used in the OCT is only attenuated 76% as much as the light in the OCM. This numerical result is consistent with the enhanced depth penetration seen in OCT images (Compare Fig. 10 with Fig. 4B).

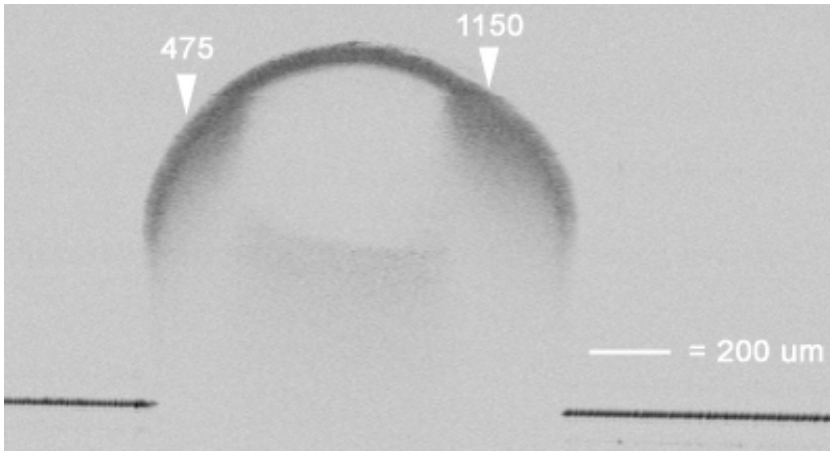


**Figure 10** 1310 nm grayscale OCT image of an embryo showing locations on the surface beneath which attenuation coefficients were determined. The values represent positions in microns relative to the left edge of the image.

**Table 2** Attenuation coefficients of *Xenopus* gastrula using 1310 nm OCT

| Position relative to left edge of image | Attenuation Coefficient ($mm^{-1}$) |
|---|---|
| 420 | 13.3 |
| 450 | 15.9 |
| 475 | 17.3 |
| 1150 | 13.8 |
| 1200 | 12.4 |
| 1240 | 11.3 |
| 1250 | 15.2 |
| 1261 | 12.5 |
| | Average: 14.0 ± 2.0 |

## DISCUSSION

We have used a non-invasive, non-destructive biological imaging technique to document events that occur internally within *Xenopus laevis* embryos undergoing gastrulation. Specifically, we have resolved the internal migration of the mesoderm, one

of the most critical events in embryonic morphogenesis. This was accomplished using inherent cellular scattering properties and without the use of exogenous labeling agents. The results presented here are in close agreement with other published accounts of *Xenopus* gastrulation (Keller, 1975; Keller, 1976), but our imaging technique is non-destructive and does not require the sacrifice of any embryos to document and describe developmental events. The resolution of internal morphological changes is especially impressive because the *Xenopus* embryo is not transparent. These findings suggest that OCM is a valuable tool in animal developmental biology.

The OCM and OCT time-lapse movies both represent descriptive and useful accounts of gastrulation. An advantage of using OCM over OCT is the third spatial dimension. The movies discussed above are evidence that several movies generated from the same data set from different perspectives (representative sections shown in Figs. 6 & 8) can offer a powerful description of development when taken together. The use of three-dimensional time-lapse OCM movies is truly effective at capturing the spatial and temporal complexities of early development; for instance, we have used the OCM images to estimate the rate of mesoderm migration to be $3.2 \pm 0.7$ μm / min. The application of this biological imaging technology extends beyond descriptive accounts of normal development. For instance, OCM could be used to follow developmental mutants as they undergo gastrulation. Also, using the sample holder (Fig. 3), we plan to orient the embryo with the vegetal hemisphere positioned upwards to image pregastrular tissue movements such as vegetal rotation, the recently described yolk mass distortion that is involved in initiating mesodermal involution (Winklbauer and Schurfeld, 1999).

The images discussed here were acquired from embryos oriented naturally with their animal pole directed upwards. This orientation offers a view of the animal hemisphere in which the ectoderm, blastocoel, and the top portion of the yolk may be readily identified. It is difficult to reliably image much of the yolk from this perspective, since the overlying ectoderm has already attenuated much of the signal. This loss of signal is quantified by determining the attenuation coefficient of the different tissue layers. The average attenuation coefficients in the ectoderm ($18.3 \pm 3.0$ mm$^{-1}$) and in the mesoderm ($19.2 \pm 5.0$ mm$^{-1}$) agree within uncertainties. The consistency of these results is not surprising since these tissues are not likely to have differentiated enough to exhibit markedly different scattering properties. Therefore, we may conclude that the blue appearance of the mesoderm in OCM images (Figs. 4B & 6) is not owing to different scattering properties between the ectoderm and mesoderm, but rather to the fact that the signal that reaches the mesoderm is already highly attenuated by the ectoderm.

These high attenuation coefficient values are indicative of the opacity of *Xenopus* embryos. This is likely owing to the fact that the scattering properties do not vary much as a function of position within embryonic *Xenopus*, as the cells are not highly differentiated. As the embryos develop into larvae they become considerably more transparent. Transparency is correlated with a lack of scatterers, and consequently OCM is able to penetrate deeper into the sample (Hoeling *et al*., 2000). In these later stages, the attenuation coefficient falls as low as 10.0 mm$^{-1}$ (data not shown). The high attenuation coefficients are the cause of the depth limitation in imaging embryonic *Xenopus* by OCM; however, the average attenuation coefficients determined from the OCT images (14.0 mm$^{-1}$) at 1310 nm suggest that a light source with a longer

wavelength provides a 36% better depth penetration within *Xenopus* embryos due to the longer wavelength. The use of a 1310 nm light source will be a consideration in the design of future instruments, but more careful observation of the embryos is necessary to ensure that the microscope remains non-destructive at higher intensities.

Future OCM designs might appropriate the Doppler-shift technology of the OCT as well, which provides the Doppler phase shift and phase shift variance images shown above (Fig. 7). When the phase shift and phase shift variance images were viewed in conjunction with the traditional backscatter image, it was apparent that there was no directed flow of any cellular components along the animal-vegetal axis (data not shown). This was indicated by the black appearance of the phase shift images. The phase shift variance images, however, indicated that there was a wide range of random, non-directed motion occurring solely within the endoderm. This is likely owing to the diffusion of platelets within the endodermal yolk cells. Yolk platelets are round structures on the order of 1 μm and thus represent likely candidates for the source of this motion (A Ewald & R. Haskell, personal communications).

Analyses of the OCT and OCM images suggest that neither microscope is well suited to resolving fine intracellular details. An additional direction for future research could involve the development of an injectible labeling agent to follow the motion of individual cells during gastrulation. The physical principles behind OCM render it insensitive to conventional fluorescent labeling agents that are widely used in fluorescence confocal microscopy. However, a scattering agent could be utilized that either strongly scatters light in the backward direction or absorbs it altogether. The strongly scattering marker would introduce brighter spots in the tissue owing to a

predominance of objects that are optimally back scattering. Mie scattering theory predicts that particles with diameters of approximately 500 nm are good candidates (van de Hulst, 1981). Alternatively, a marker that strongly absorbed light at the wavelength of the light source would produce a black portion of the tissue. This also would lead to a shadowing effect on the tissue beneath it, but it could still provide a means for following small groups of cells. A third alternative could exploit the fact that 1 μm particles such as yolk platelets undergo random diffusion that can be readily resolved by Doppler OCM or OCT (Fig. 9). A concentrated solution of 1 μm scatterers could be injected into a population of cells and their appearance on the velocity-variance images could be view in conjunction with the traditional scattering intensity image to aid in following these cells.

OCM time-lapse movies could be used to document the events of later development as well. Previously our OCM has been used to image fixed frogs at larval stages of development (Hoeling *et al.*, 2000). These images show a wealth of complex structures such as the notochord, spinal cord, somites and other structures of the developing musculature and nervous system. Since these structures can be resolved at later stages, presumably their formation could be documented as well.

## ACKNOWLEDGEMENTS

I would like to acknowledge my advisors at Harvey Mudd (Drs. Mary Williams, Richard Haskell and Daniel Petersen) and at Caltech (Drs. Scott Fraser and Cyrus Papan). I am also indebted to the support of Drs. Hongwu Ren and Zhongping Chen of the Beckman Laser Institute at UC Irvine for use of their OCT. I would like to thank all members of Team OCM over the years, as well as the Beckman Foundation for funding a

significant portion of this research. Finally, I acknowledge the Harvey Mudd College Departments of Biology and Physics.

## REFERENCES

Bernardini G, Prati M, Bonetti E, Scari G. 1999. *Atlas of* Xenopus *Development*. Milano: Springer-Verlag Italia.

Boppart S, Tearney G, Bouma B, Southern J, Brezinski M, Fujimoto J. 1996. Investigation of developing embryonic morphology using optical coherence tomography. *Dev Biol* 177: 54-63.

Boppart S, Tearney G, Bouma B, Southern J, Brezinski M, Fujimoto J. 1997. Noninvasive assessment of the developing *Xenopus* cardiovascular system using optical coherence tomography. *Proc Natl Acad Sci USA*. 94: 4256-4261.

Boppart SA, Bouma BE, Pitris C, Southern JF, Brezinski ME, Fujimoto JG. 1998. In vivo cellular optical coherence tomography imaging. *Nat Med* 4: 861-865.

Fraser SE, Harland RM. 2000. The Molecular Metamorphosis of Experimental Embryology. *Cell* 100: 41-55.

Fujimoto JG, Bouma B, Tearney GJ, Boppart SA, Pitris C, Southern JF, Brezinski ME. 1998. New technology for high-speed and high-resolution optical coherence tomography. *Ann N Y Acad Sci*. 9(838): 95-107.

Gurses-Ozden R, Ishikawa H, Hoh ST, Liebmann JM, Mistlberger A, Greenfield DS, Dou HL, Ritch R. 1999. Increasing sampling density improves reproducibility of optical coherence tomography measurements. *J Glaucoma*. 1999 8(4):238-41.

Haseloff J. 1999. GFP variants for multispectral imaging of living cells. *Methods Cell Biol*. 58: 139-151.

Hausen P, Riebesell M. 1991. *The Early Development of* Xenopus Laevis: *An Atlas of the Histology.* New York: Springer-Verlag.

Heasman J. 1997. Patterning the *Xenopus* blastula. *Development* 124: 4179-4191.

Herman B, Lemasters JJ. 1993 Laser scanning confocal microscopy of living cells. *Optical Microscopy: Emerging Methods and Applications*. Academic Pr: San Diego.

Hettinger JW, Mattozzi MdlP, Myers WR, Williams ME, Reeves A, Parsons RL, Haskell RC, Petersen DC, Wang R, Medford JI. 2000. Optical Coherence Microscopy: A Technology for Rapid, in Vivo, Non-Destructive Visualization of Plants and Plant Cells. *Plant Physiology* 123(1): 3-16

Hoeling BM, Fernandez AD, Haskell RH, Huang E, Myers WR, Petersen DC, Ungersma SE, Wang R, Williams ME, Fraser SE. 2000. An optical coherence microscope for 3-dimensional imaging in developmental biology. *Optics Express* 6: 136-146.

Izatt JA, Kulkarni MD, Wang H, Kobayashi K, Sivak MV. 1996. Optical Coherence Tomography and Microscopy in Gastrointestinal Tissues. *IEEE Journal of Selected Topics in Quantum Electronics*. 2(4): 1017-1028.

Jacobs RE, Ahrens ET, Meade TJ, Fraser SE. 1999. Looking deeper into vertebrate development. *Trends in Cell Biology*. 9(2): 73-76.

Keller RE. 1975. Vital dye mapping of the gastrula and neurula of *Xenopus laevis* I. Prospective areas and morphogenetic movements of the superficial layer. *Developmental Biology*. 42, 222-241.

Keller RE. 1976. Vital Dye Mapping of the gastrula and neurula of *Xenopus laevis* II *Developmental Biology*. 51, 118-137.

Keller RE. 1980. The cellular basis of epiboly: an SEM study of deep-cell rearrangement during gastrulation in *Xenopus laevis*. *J Embryol Exp Morphol*. 60:201-34.

Keller RE. 1991. Early Embryonic Development. *Methods in Cell Biology:* Xenopus laevis*: Practical Uses in Cell and Molecular Biology*. Academic Press: San Diego, pp 61 – 113.

Louie AY, Hueber MM, Ahrens ET, Rothbacher U, Moats R, Jacobs RE, Fraser SE, Meade TJ. 2000. In vivo visualization of gene expression using magnetic Resonance imaging. *Nature Biotechnology*. 18(3): 321-325.

Mourant JR, Canpolat M, Brocker C, Esponda-Ramos O, Johnson TM, Matanock A, Stetter K, Freyer JP. 2000. Light scattering from cells: the contribution of the nucleus and the effects of proliferative status. *J. Biomedical Optics*. 5(2): 131-137.

Paddock SW. 1999. Confocal laser scanning microscopy. *Biotechniques*. 27: 992-1004.

Peng HB. 1991. Solutions and Protocols. *Methods in Cell Biology:* Xenopus laevis*: Practical Uses in Cell and Molecular Biology*. Academic Press: San Diego, pp 657 – 662.

Van de Hulst HC. 1981. *Light Scattering by Small Particles*. Toronto: General Publishing Company, Ltd.

Van Holde, K. 1971. *Physical Biochemistry*. Englewood Cliffs: Prentice-Hall, Inc.

Winklbauer, R, Schurfeld, M. 1999. Vegetal rotation, a new gastrulation movement involved in the internalization of the mesoderm and endoderm in *Xenopus*. *Development*. 126: 3703-3713.

Wu M, Gerhart J. 1991. Raising *Xenopus* in the Laboratory. Methods in Cell Biology: *Xenopus laevis*: Practical Uses in Cell and Molecular Biology. Academic Press: San Diego, pp 3 – 18.

Zhao YH, Chen ZP, Saxer C, Xiang SH, deBoer JF, Nelson JS. 2000. Phase-resolved optical coherence tomography and optical Doppler tomography for imaging blood flow in human skin with fast scanning speed and high velocity sensitivity. *Optics Letters*. 25: 114-116.